Journal of
Materials Chemistry A

ROYAL SOCIETY
OF CHEMISTRY

PAPER

View Article Online
View Journal | View Issue

Check for updates

Cite this: *J. Mater. Chem. A*, 2023, **11**, 22478

Nano *vs.* bulk: surfactant-controlled photophysical and morphological features of luminescent lanthanide MOFs†

Moritz Maxeiner,[a] Lea Wittig,[a] Alexander E. Sedykh,[a] Thomas Kasper[a] and Klaus Müller-Buschbaum *[ab]

A surfactant-assisted bottom-up synthesis route provides access to nanoscale metal–organic frameworks (nMOFs) that exploit size-dependent property advantages. This includes an increased surface-to-volume ratio, improved dispersibility and superior morphological properties by a narrow size distribution compared to the bulk analogues. Photophysical properties such as photoluminescence are also influenced by particle size, surfactant components and post-synthetic modification. The series of the related organic linkers (H_2bdc, H_2bpdc and H_2bpydc) together with trivalent lanthanides (Ln^{3+} = Eu^{3+}, Tb^{3+}) in synthesis and post-synthetic modification together with surface-active agents (CTAB, PVP) were used to assemble luminescent nMOFs for three archetype MOFs: nLn^{3+}-bdc, nDUT-5:Ln^{3+} and nMOF-253:Ln^{3+}. Both, dispersibility and morphology benefit from the CTAB- and PVP-controlled bottom-up particle downsizing down to 35 nm. DLS confirms homogeneous, narrow particle size distributions down to ±5 nm, which is 21-times smaller than the bulk analogues. Moreover, excellent luminescence QYs of up to 78.1(3)% were determined for the Ln^{3+}-containing nMOFs. Successful post-synthetic modification with trivalent lanthanide ions of nMOFs was accomplished showing an improved photoluminescence sensitization effect compared to the bulk MOFs and exhibiting increased Ln^{3+}-to-linker emission intensity ratios. The amount and photophysical properties of surfactants encapsulating the nMOFs were further quantified by DTA/TG-MS and UV-Vis-DRS. Finally, this work aims to elaborate thoroughly on the previously mentioned properties of nMOFs by comparison with their bulk analogues. Since surfactants play a key role in this synthesis route, the pros and cons of this approach were also assessed concerning several nMOF features.

Received 30th August 2023
Accepted 8th October 2023

DOI: 10.1039/d3ta05219b

rsc.li/materials-a

Introduction

Metal–organic frameworks (MOFs) combine a wide variety of chemical adaptability with intrinsic potentially occupiable interstices, leading to a vast range of applications such as gas storage,[1–3] medical implementation,[4–6] catalysis,[7–9] sorption matrix,[10–12] sensors[13–15] or ionic conductors.[16–18] The ability to play a role in such a variety of applications is given by the vast possibility of combinations of various inorganic building units (IBUs) and organic linkers. The properties of MOFs strongly depend on the structure, electronic states, functional groups, and synthesis parameters, making MOFs highly tuneable porous materials.[19] Trivalent lanthanide (Ln^{3+})-containing MOFs are of a particular interest, as their unique photophysical properties render them highly suitable for the use as optical sensors.[20–22] The light uptake by direct excitation of Ln^{3+} ions is low, due to the non-binding character of electronically isolated 4f-orbitals and the parity-prohibition of 4f–4f transitions according to Laporte's rule.[23,24] However, the light uptake of Ln^{3+} can be significantly enhanced indirectly by a proper organic linker capable of a high light absorption followed by an energy transfer to Ln^{3+} ions, from which light is emitted. Thereby, this 'antenna effect' or 'sensitization' overall enhances the luminescence properties of the composite material.[25] This includes lanthanide ions inside MOF pores.[26] The range of emitted light covers both, the vis-region from 400 nm to 800 nm and also the NIR-region from 800 nm to 1700 nm is possible.[27] This is an interesting endorsement of the photophysical capability of lanthanide MOFs and provides excess to applications such as luminescent MOF barcodes.[28]

The interest in nanoparticles has grown enormously over the last two decades due to their unique size-dependent properties, which can be readily influenced by limiting their particle growth. As a result, they outperform their bulk analogues with

---

[a] *Institute of Inorganic and Analytical Chemistry, Justus-Liebig-University Giessen, Heinrich-Buff-Ring 17, 35392 Giessen, Germany. E-mail: kmbac@uni-giessen.de; Web: **https://www.uni-giessen.de/de/fbz/fb08/Inst/iaac/mueller-buschbaum***

[b] *Center for Materials Research (LAMA), Justus-Liebig-University Giessen, Heinrich-Buff-Ring 16, 35392 Giessen, Germany*

† Electronic supplementary information (ESI) available. See DOI: **https://doi.org/10.1039/d3ta05219b**

higher surface-to-volume ratios, increased solvent affinity, enhanced particle penetration rates, and newly acquired photophysical properties.[29] Nowadays, the importance of functionalized nanomaterials extends to a multitude of sectors, for instance, electronics[30–32] and medical applications.[33–35] However, the generation of novel nanomaterials is still challenging, as inevitable processes such as Ostwald ripening or agglomeration must be overcome. Therefore, well-designed synthesis routes with size limiting features are required. Several methods have been established using either chemical additives or physical concepts in bottom-up and top-down routes, respectively.[36,37]

The contradicting idea of reducing an extended three-dimensional network in size, which is defined by its long-range order, crystallinity, and an enormous number of pores as in bulk MOFs, consequently, takes these specific properties away but leads to nano-scaled MOF (nMOF) particles consisting of only a couple of unit cells. Furthermore, nMOFs offer the advantages stated above of bulk MOFs, plus those given by their nano-character.[38] The bottom-up downsizing results in a higher specific surface area and less gravitational influence on dispersibility compared to bulk MOFs, as well as defined optical properties through the incorporation of luminophores.[39] Therefore, distinct improvements can be achieved in the synthesis and application of composites containing nLn^{3+}-MOFs compared to their bulk analogues. For instance, enhanced homogeneity and stability of a dispersion or ameliorated sorption efficiency.

In principle, nLn^{3+}-MOFs can be synthesized by a bottom-up[40] or top-down approach.[41] In this work, the bottom-up approach implements a template-based method by using surface-active agents (surfactants).[42] Scheme 1 shows the behaviour of the cationic tenside *N*,*N*,*N*-trimethylhexadecan-1-ammonium bromide (CTAB) and polyvinylpyrrolidone (M_w = 40 000 g mol^{-1}, $PVP_{40\,000}$) in solution prior to the synthesis of the nMOF, enclosing both the IBU (Ln^{3+} or Al^{3+}) and the deprotonated linker in a confined synthesis space, which is the key to yield nMOFs and the method of choice in this work.

Ln^{3+} were incorporated into MOFs either during the MOF synthesis or by post-synthetic modification of the synthesized MOF. The Ln^{3+}-bdc ($Ln^{3+} = Eu^{3+}, Tb^{3+}$) has been prepared by mixing Eu^{3+}- or Tb^{3+}-salts as IBU with benzene-1,4-dicarboxylic acid (H_2bdc) as linker. For the post-synthetic modification approach, MOFs have been synthesized with Al^{3+}-salts as IBU with biphenyl-4,4′-dicarboxylic acid (H_2bpdc) or 2,2′-bipyridine-5,5′-dicarboxylic acid (H_2bpydc) as linkers. These MOFs are hereafter referred to as DUT-5:Ln^{3+} and MOF-253:Ln^{3+} ($Ln^{3+} = Eu^{3+}, Tb^{3+}$) according to their impregnation with Eu^{3+} ions or Tb^{3+} ions. An overview of the MOFs used in this work and the type of Ln^{3+}-incorporation is given in Table 1.

A variety of analytical techniques were used to fully characterize the systems. Powder X-ray diffraction (PXRD), dynamic light scattering (DLS), scanning electron microscopy (SEM), microwave plasma – atomic emission spectroscopy (MP-AES), organic elemental analysis (OES) and simultaneous differential thermoanalysis/thermogravimetry combined with mass spectrometry (DTA/TG-MS) were carried out to entirely characterize the structure, composition, and particle morphology. In order to provide photophysical data, a spectrophotometer was used equipped with different setups for

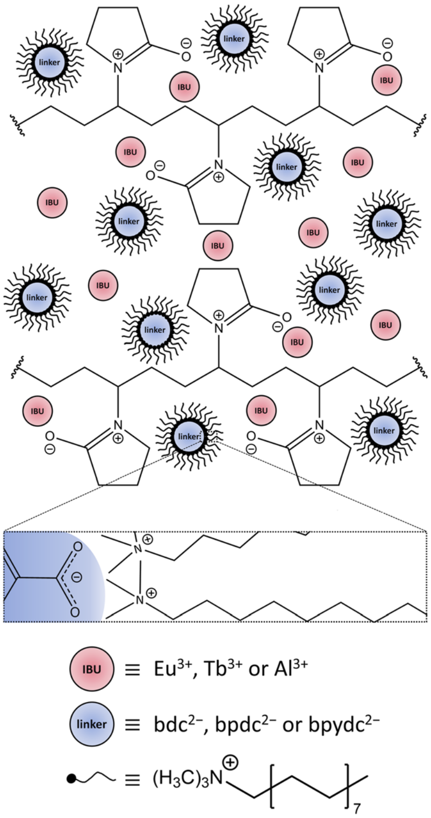

Scheme 1 Depiction of the confined space made up by the surfactants CTAB and $PVP_{40\,000}$, enclosing the IBU and linker ions prior to the synthesis. Red circles represent the IBU cations Eu^{3+} for Eu^{3+}-bdc, Tb^{3+} for Tb^{3+}-bdc, and Al^{3+} for DUT-5 and MOF-253, respectively. Blue circles represent the deprotonated linkers bdc^{2-}, $bpdc^{2-}$ and $bpydc^{2-}$ for Ln^{3+}-bdc, DUT-5 and MOF-253, respectively. The linkers are surrounded by black, tailed symbols representing reverse micelles, which are formed by CTAB. The enlarged rectangular box shows Coulomb-attraction between the negatively charged carboxylate group of the linker and the positively charged ammonium part of the CTAB in more detail. $PVP_{40\,000}$ forms layers enclosing a limited amount of IBU and the linker-containing reverse micelles. Both, CTAB and $PVP_{40\,000}$ set up the steric synthesis parameters for nMOFs. Solvent molecules, NO_3^- and Br^- counterions have been omitted for clarity. The dimensions do not correspond to reality.

Table 1 MOF nomenclature with respect to IBU, linker and Ln^{3+} incorporation approach

MOF[a]	IBU	Linker	Ln^{3+} incorporation approach
Eu^{3+}-bdc	Eu^{3+}	H_2bdc	Synthesis
Tb^{3+}-bdc	Tb^{3+}		
DUT-5	Al^{3+}	H_2bpdc	—
DUT-5:Ln^{3+}			Post-synthetic
MOF-253		H_2bpydc	—
MOF-253:Ln^{3+}			Post-synthetic

[a] Nomenclature is valid for both bulk MOF and nMOF.

excitation and emission spectra (PL), luminescence decay (lifetime τ), quantum yield (QY) and linker triplet state determination. A UV-Vis diffuse reflectance spectrophotometer (UV-Vis-DRS) complemented the photophysical data acquisition.

For this work, three archetype MOFs were both synthesized as bulk (Ln^{3+}-bdc, DUT-5, MOF-253, the latter two were post-synthetically modified with Ln^{3+}: DUT-5:Ln^{3+}, MOF-253:Ln^{3+}) and nano (nLn^{3+}-bdc, nDUT-5:Ln^{3+}, nMOF-253:Ln^{3+}) batch materials and discussed concerning their properties. A comparison of bulk MOFs and nMOFs on morphological and photophysical properties reveals the potential of nanomaterials.

Results and discussion

Crystal structures of Ln^{3+}-bdc, DUT-5 and MOF-253

The successful bottom-up surfactant-assisted downsizing of Ln^{3+}-bdc, DUT-5 and MOF-253 to nMOFs has been confirmed by PXRD in terms of crystallinity, purity, and potential side phases. Fig. 1 shows the PXRD results of nLn^{3+}-bdc, nDUT-5 and nMOF-253 as well as the simulated diffractograms for the single-crystal data of Ln^{3+}-bdc, DUT-5 and MOF-253, respectively. Moreover, the diffractograms of the corresponding bulk MOFs are shown in Fig. SI3–6.† All synthesized bulk MOFs and nMOFs correspond to the simulated powder patterns based on single crystal structure data. The crystal structures of the archetype MOFs Tb^{3+}-bdc,[43] DUT-5 [44] and MOF-253 [45] are well known (for clarity, they are depicted in Fig. SI1 and 2†). PXRD reveals nEu^{3+}-bdc and nTb^{3+}-bdc to be isostructural and therefore called nLn^{3+}-bdc (with Ln^{3+} = Eu^{3+}, Tb^{3+}). While the crystal structures of nDUT-5 and nMOF-253 are directly related. A broadening of the reflections is apparent for all nMOFs compared to the diffraction patterns of their bulk analogues. This can be explained by the reduction of crystallinity due to the decrease in particle size. The described phenomenon was already previously observed for other nMOFs.[46] However, crystallite size determination using the Scherrer equation is not applicable due to broad, unseparated reflections. A slight overall shift of 2θ is noticeable in the diffractograms of MOF-253 and nMOF-253 compared to the simulated powder pattern of MOF-253, which was also previously observed by Deng *et al.* for the archetype MOF-253.[47]

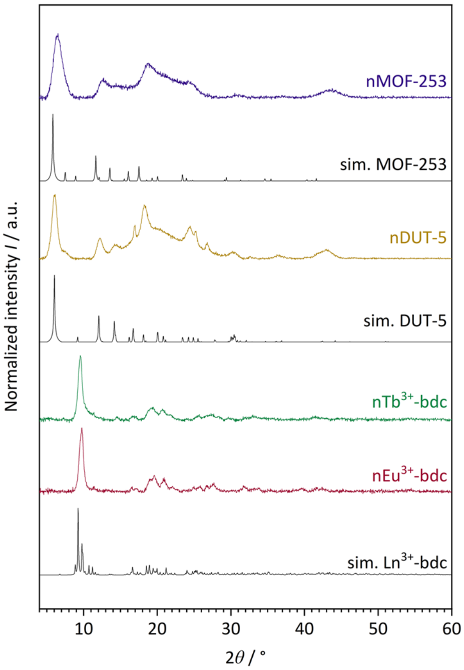

Fig. 1 Experimental powder patterns of the investigated nMOFs: nEu^{3+}-bdc, nTb^{3+}-bdc, nDUT-5 and nMOF-253. Furthermore, simulated (sim.) powder patterns for single crystal data of Tb^{3+}-bdc,[43] DUT-5 (ref. 44) and MOF-253 (ref. 45) are shown. Since nEu^{3+}-bdc and nTb^{3+}-bdc are isostructural they are denoted as Ln^{3+}-bdc (with Ln^{3+} = Eu^{3+}, Tb^{3+}). Both, experimental and single crystal data were acquired at room temperature and at ambient air atmosphere.

Noteworthy is a broad reflection between 15–30° for nDUT-5 and nMOF-253, which belongs to the surface-located CTAB. This was also shown by Chhetri *et al.* for CTAB-functionalized MoS_2. They described both CTAB attached and intercalated to the surface and in between MoS_2 nanolayers, respectively.[48] In our work, the cationic tenside CTAB forms reversible reverse micelles due to Coulomb-interactions with the unsaturated anionic carboxylate groups at the MOF surface. In contrast to micelles, the hydrophilic heads of reverse micelles face the centre, while at the outside, the tails form a hydrophobic interface with the solvent. A dynamic process of enclosing the MOF is essential to allow MOF synthesis. But the surfactant limits particle growth and also affects particle shape and dispersibility.[49,50] Moreover, the presence of small amounts of residual amorphous polymer $PVP_{40\,000}$ cannot be excluded by PXRD since this method is sensitive to the diffraction of crystalline materials only and therefore unable to detect thin layers of amorphous materials as $PVP_{40\,000}$. In fact, $PVP_{40\,000}$ forms non-linear layers in solution that resemble a confined space synthesis by encapsulating all the reactants. Particle growth becomes limited and unidirectional due to the limited amount of IBU and linker within this space.[51]

Besides, the results do not show reflections of the reagents, side phases or other non-assignable reflections, respectively.

Composition and morphology

Characterisation of non-post-synthetically modified bulk MOFs and nMOFs. DLS reveals successful particle size reduction and more homogeneous, narrower particle size distributions of the nMOFs compared to the corresponding bulk MOFs. An overview of particle sizes and their distributions is shown in Fig. 2 and stated in Table 2. DLS gives 125 ± 40 nm for nEu^{3+}-bdc (Fig. 3b), 90 ± 35 nm for nTb^{3+}-bdc (Fig. 3d), 35 ± 5 nm for nDUT-5 (Fig. 3f) and 90 ± 20 nm for nMOF-253 (Fig. 3h), respectively. It needs to be considered that DLS measures the hydrodynamic radius of the nMOFs, which includes the surrounding surfactant as well as solvent molecules bound by electrostatic interactions to the nMOF and therefore leads to larger particles than the determination by electron microscopy (20–60 nm for Ln^{3+}-bdc, 10–20 nm for nDUT-5 and 15–30 nm for nMOF-253). SEM images confirm homogenous nLn^{3+}-bdc (Fig. 3a and c), nDUT-5 (Fig. 3e) and nMOF-253 (Fig. 3g) particles in terms of size distribution and shape. However,

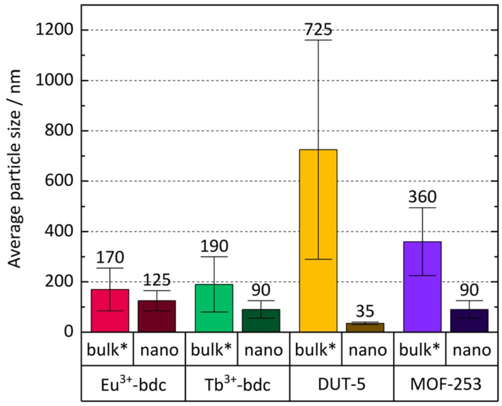

Fig. 2 Comparison of average particle size and particle size distribution (error bars) of Ln^{3+}-bdc, nLn^{3+}-bdc (Ln^{3+} = Eu^{3+}, Tb^{3+}), DUT-5, nDUT-5, MOF-253 and nMOF-253. Bulk MOF sizes supposed to be larger than stated due to an unavoidable sedimentation of larger particles in the dispersion during the DLS measurement and are therefore marked with an asterisk.

nanoparticle boundaries become blurred for nDUT-5 and nMOF-253 due to an increased amount of surfactants.

Bulk MOF synthesis results in clefted microparticles (>400 nm) for Ln^{3+}-bdc, and spherical particles (>1000 nm) for DUT-5 and MOF-253, respectively, as SEM demonstrates. Furthermore, particle size determination based on DLS reveals particles sizes of 170 ± 85 nm for Eu^{3+}-bdc, 190 ± 110 nm for Tb^{3+}-bdc, 725 ± 430 nm for DUT-5 and 360 ± 135 nm for MOF-253. However, bulk MOF particle sizes again supposed to be even higher due to an unavoidable sedimentation process during the DLS data acquisition (Fig. SI10†).

As PXRD and SEM already indicated the presence of surfactants at the outside of the nMOFs, coverage with PVP$_{40\,000}$ as well as the reverse micelle formation of CTAB lead to narrow particle size distributions and smaller particle sizes (Fig. 3b, d, f and h). In addition and beneficially, a dispersion with nMOFs is stabilized by residual surfactants and prevents sedimentation during DLS data acquisition. Scheme 2 illustrates how the surfactants are enclosing a nMOF particle which leads to the stabilization effect. It should be emphasized that nDUT-5 particles were significantly reduced in size by a factor of ≈21 and remarkably homogenized compared to DUT-5 (see Fig. 2).

Further information on the presence of surfactants on bulk MOFs and nMOFs was obtained by DTA/TG-MS using synthetic air as the working gas, which can oxidize the MOF instead of typical inert gases such as Ar/N$_2$. DTA/TG-MS results are shown in Fig. 4 and as enlarged graphics in Fig. SI14–16 in the ESI.† DTA/TG confirm an exothermic mass loss of 15 wt% and 7 wt% for Tb^{3+}-bdc (Fig. 4a) and nTb^{3+}-bdc (Fig. 4b), respectively, at 230–270 °C. MS signals identify these mass losses as the solvent molecules H_2O and DMF either located in the pores or at the surface of the MOFs. The mass loss of DUT-5 (Fig. 4c) with 40 wt% is higher than the mass loss of nDUT-5 (Fig. 4d) with 10 wt% at 100–250 °C. Consequently, both nTb^{3+}-bdc and nDUT-5 contain less solvents than their bulk analogues, suggesting that surfactants partially replace solvents in the pores and on the surface of nMOFs.

Table 2 Overview of quantitative data for the investigated Ln^{3+}-bdc, nLn^{3+}-bdc, DUT-5:Ln^{3+}, nDUT-5:Ln^{3+}, MOF-253:Ln^{3+} and nMOF-253:Ln^{3+} (Ln^{3+} = Eu^{3+}, Tb^{3+})

		Particle size/nm			Wavelength λ_{max}/nm		QY/%		Lifetime τ/ms	
		DLS[a]								
	Ln^{3+}/wt%	MeCN	EtOH	SEM	PL ex	PL em	Ln^{3+}	Linker	τ_1	τ_2
Eu^{3+}-bdc	32	n/a[g]	170 ± 85	>1000	288	614	33(2)	n/a[e]	0.9055(6)	n/a[f]
nEu^{3+}-bdc	32	n/a[g]	125 ± 40	20–60	296	614	23.7(3)	n/a[e]	0.701(4)	1.071(3)
Tb^{3+}-bdc	38	n/a[g]	190 ± 110	>1000	300	544	94(2)	n/a[e]	1.396(2)	n/a[f]
nTb^{3+}-bdc	33	n/a[g]	90 ± 35	20–60	286	543	78.1(3)	n/a[e]	1.04(4)	1.612(3)
DUT-5	n/a[c]	n/a[g]	725 ± 430	>400	307	376[b]	n/a[c]	5.1(5)	$2.49(6) \times 10^{-6}$	n/a[f]
nDUT-5	n/a[c]	n/a[g]	35 ± 5	10–20	326	378[b]	n/a[c]	14.8(6)	$3.6(1) \times 10^{-6}$	n/a[f]
DUT-5:Eu^{3+}	2	265 ± 115	500 ± 90	>400	307	616	2.1(2)	10.4(3)	0.288(6)	0.596(6)
nDUT-5:Eu^{3+}	2	175 ± 55	110 ± 10	20–50	310	616	3.6(1)	4.5(3)	0.306(8)	0.70(1)
DUT-5:Tb^{3+}	2	290 ± 110	385 ± 260	>400	416	544	n/a[d]	11.5(3)	n/a[d]	n/a[d]
nDUT-5:Tb^{3+}	1	160 ± 35	105 ± 10	20–50	427	544	n/a[d]	4.6(2)	n/a[d]	n/a[d]
MOF-253	n/a[c]	n/a[g]	360 ± 135	>400	370	440[b]	n/a[c]	<1	$1.19(6) \times 10^{-6}$	$6.4(1) \times 10^{-6}$
nMOF-253	n/a[c]	n/a[g]	90 ± 20	15–30	366	536[b]	n/a[c]	<1	$0.559(7) \times 10^{-6}$	$2.13(5) \times 10^{-6}$
MOF-253:Eu^{3+}	3	185 ± 180	150 ± 60	>400	327	616	2.0(1)	n/a[e]	0.204(3)	0.432(3)
nMOF-253:Eu^{3+}	4	135 ± 70	155 ± 80	20–50	310	616	1.79(3)	n/a[e]	0.14(2)	0.308(6)
MOF-253:Tb^{3+}	7	155 ± 70	130 ± 45	>400	374	544	n/a[d]	<1	n/a[d]	n/a[d]
nMOF-253:Tb^{3+}	2	100 ± 10	155 ± 70	20–50	371	544	n/a[d]	<1	n/a[d]	n/a[d]

[a] Particle sizes of bulk MOFs are supposed to be even higher due to sedimentation. [b] Recording of linker-based emission spectrum. [c] No Ln^{3+} present in the sample. [d] Only linker-based emission observable, no sufficient energy transfer from linker to Tb^{3+}. [e] No linker-based emission intensity observable in PL spectra. [f] An exponential fit of first order was used. [g] Measurements not carried out in MeCN.

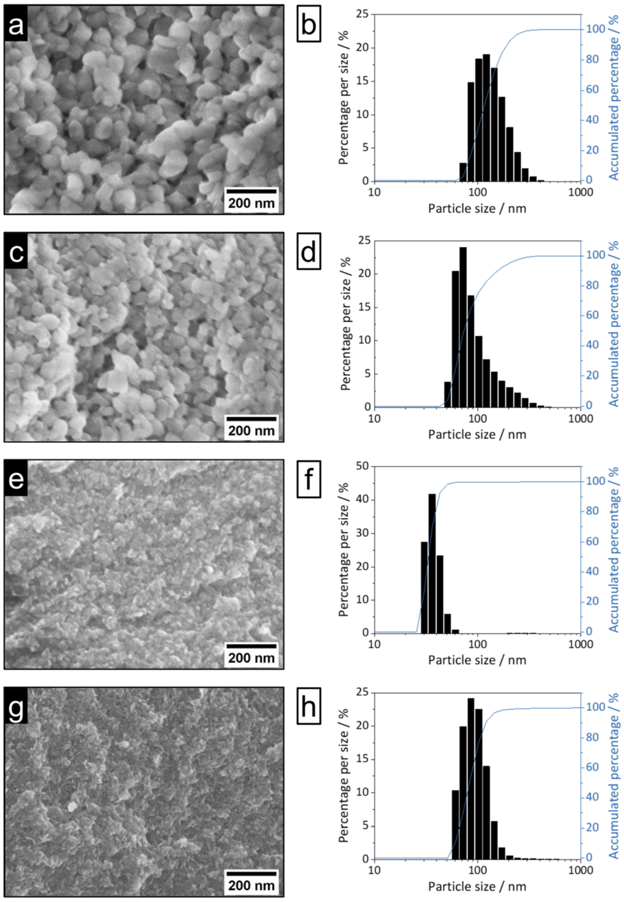

Fig. 3 SEM images (100k magnification, left) and DLS particle size distributions (right) of nEu^{3+}-bdc (a and b), nTb^{3+}-bdc (c and d), nDUT-5 (e and f) and nMOF-253 (g and h).

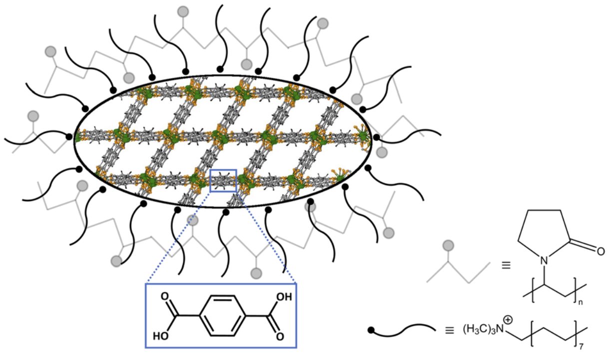

Scheme 2 Depiction of a surfactant-stabilized nMOF particle. The Tb^{3+}-bdc crystal structure is shown within the particle-shaped area and represents the MOFs used. Atom color code: green (Tb), yellow (O), grey (C), black (H). The nMOF is surrounded by black, tailed symbols representing reverse micelles, which are formed by CTAB. PVP$_{40\,000}$ impacts the particle shape by enclosing the nMOF depicted as pale-grey chains. The blue box shows exemplarily the H_2bdc in Tb^{3+}-bdc as representative for the linkers used.

In Fig. 4b, mass losses of 1 wt% at 305–345 °C and 13 wt% at 400–500 °C were observed for nTb^{3+}-bdc, attributed to the oxidation of CTAB and PVP$_{40\,000}$, respectively. Results from MS allow for the identification of CO_2, NO and H_2O as oxidation products, confirming the oxidation of surfactants, for the deprotonated linker bdc^{2-} does not contain nitrogen. In the oxidation process, a shorter aliphatic chain as in CTAB requires less energy to be cracked than a longer polymeric chain as in PVP$_{40\,000}$. In fact, this effect has been previously reported for CTAB[52] and PVP$_{40\,000}$ (ref. 53) for the above-mentioned temperature ranges. The powder pattern of nTb^{3+}-bdc does not show any broad reflection at 12–30° (Fig. 1), therefore the amount of surfactant must be lower than for nDUT-5 and nMOF-253. In corroboration, both, nDUT-5 and nMOF-253 show a higher mass loss of 30 wt% at 300–470 °C (Fig. 4d and f). Moreover, NO signals at 310–420 °C and 300–470 °C for nDUT-5 and nMOF-253, respectively, are indicating surfactant oxidation and further confirm this assignment.

NO signals starting at 500 °C can be assigned to the oxidation of the N-containing linker bpydc^{2-} (Fig. 4e and f). Additionally, the ongoing oxidation of organic linkers is also indicated by the CO_2 signal starting at 400 °C for Tb^{3+}-bdc and nTb^{3+}-bdc while the oxidation of the linkers of DUT-5, nDUT-5, MOF-253 and nMOF-253 continues at 500 °C. The DTA/TG-MS results do not show any NO signals at 320–420 °C for the investigated bulk MOFs, thus the mass loss can be attributed to the amount of surfactants present in the investigated nMOFs by comparing bulk MOF and nMOF results.

At temperatures higher than 650 °C, Tb^{3+}-bdc and nTb^{3+}-bdc become fully oxidized accompanied by an altogether mass loss of 60 wt% with Tb_4O_7 being formed (Fig. 4a and b). Higher temperatures, starting at 850 °C are necessary to fully oxidize DUT-5 and nDUT-5 as well as MOF-253 and nMOF-253 to Al_2O_3 with an altogether mass loss of 85 wt% (Fig. 4c–f). Both, Tb_4O_7 and Al_2O_3 are confirmed as oxidation products by PXRD (Fig. SI9†).

Characterisation of post-synthetically modified bulk MOF:Ln^{3+} and nMOF:Ln^{3+}. To study the effect of post-synthetic modification with Ln^{3+} ions on the composition as well as on particle size and particle size distribution of DUT-5, nDUT-5, MOF-253 and nMOF-253, they were impregnated with solutions of Eu^{3+}- and Tb^{3+}-salts. Details of the impregnation procedure are described in the Experimental section.

The amount of Ln^{3+} was determined by MP-AES and the results are presented in Table 2. Ln^{3+}-bdc and nLn^{3+}-bdc contain 32–38 wt% Ln^{3+} depending on the lanthanide and MOF. In contrast, the post-synthetically modified DUT-5:Ln^{3+} and nDUT-5:Ln^{3+} contain only 1–2 wt% Ln^{3+}, while MOF-253:Ln^{3+} and nMOF-253:Ln^{3+} contain 2–7 wt% Ln^{3+}, again depending on lanthanide and MOF. The difference in the amount of Ln^{3+} between both synthesis approaches is explainable by the function of Ln^{3+} ions in the MOFs. As main connectivity centre, Ln^{3+} is much more present in Ln^{3+}-bdc than by impregnation of DUT-5:Ln^{3+} and MOF-253:Ln^{3+}. It can be seen that the surfactants do not have a distinct impact on the uptake of Ln^{3+} ions, as the amount of Ln^{3+} do not follow any comprehensible trend between bulk MOFs and nMOFs.

Powder patterns of DUT-5:Ln^{3+} and nDUT-5:Ln^{3+} (Fig. SI7†) as well as MOF-253:Ln^{3+} and nMOF-253:Ln^{3+} (Fig. SI8†) reveal stable crystal structures for MOF:Ln^{3+}s impregnated with Eu^{3+}

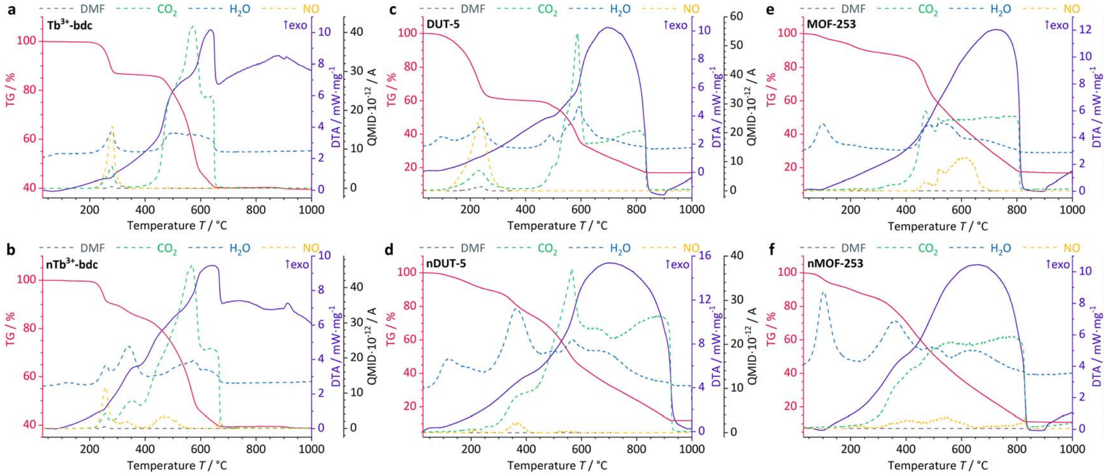

Fig. 4 DTA/TG-MS results of investigated bulk MOFs and nMOFs at synthetic air atmosphere. Tb^{3+}-bdc (a), nTb^{3+}-bdc (b), DUT-5 (c), nDUT-5 (d), MOF-253 (e) and nMOF-253 (f). NO signal (yellow) is given in QMID × 10^{-13}. A for a more detailed insight.

and Tb^{3+}. As a side effect of the post-synthetic modification process, the broad reflection at 12–30° 2θ in the diffractograms of nDUT-5 and nMOF-253 is less intense than in the diffractograms of nDUT-5:Ln^{3+} and nMOF-253:Ln^{3+}. Hence, SEM images of nDUT-5:Ln^{3+} and nMOF-253:Ln^{3+} modified in MeCN were recorded to check whether a reduced amount of surfactant can be observed. The partial purification from surfactants results in distinguishable particles for nDUT-5:Ln^{3+} and nMOF-253:Ln^{3+} (Fig. 5) meaning a lesser amount of surfactants are covering nMOF particles.

Complementary results on particle size and its distribution for the post-synthetically modified MOF:Ln^{3+} and nMOF:Ln^{3+} were obtained by DLS and are given in Table 2. DLS reveals the influence of the reduced amount of surfactants on the morphological properties and particle growth indicated by increasing particle sizes (130–140 nm for nDUT-5:Ln^{3+} and 10–50 nm for nMOF-253:Ln^{3+}, respectively, see also Fig. SI11†). Processes such as crystal growth during post-synthetic modification due to a more accessible nMOF surface, which was previously covered with surfactants, or swelling of the crystal structure due to Ln^{3+} insertion are likely to be responsible for the determined increased particle sizes. In addition, penetration of the crystal structure by surfactants or formation of holes/defects by anions to compensate for the positive charge brought in by Ln^{3+} also contribute to the swelling effect.[54] This increase in particle size is more prominent for nDUT-5:Ln^{3+} than for nMOF-253:Ln^{3+} due to the smaller particle size of nDUT-5. The smaller the particles, the higher the surface energy and the more distinct surface energy reducing mechanisms become, such as Ostwald-ripening, which consequently leads to crystal growth.[55] In addition, bulk MOF:Ln^{3+} particle sizes are hardly comparable with non-modified bulk MOF particle sizes due to sedimentation processes described above during the DLS data acquisition, and therefore, do not follow any discernible trend (Fig. SI12 and 13†).

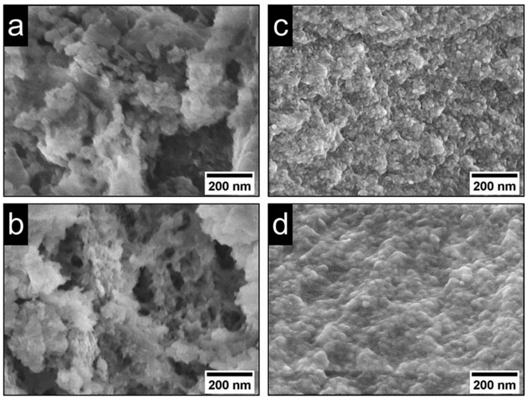

Fig. 5 SEM images (100k magnification) of (a) nDUT-5:Eu^{3+}, (b) nDUT-5:Tb^{3+}, (c) nMOF-253:Eu^{3+} and (d) nMOF-253:Tb^{3+}.

Altogether, these results point to the presence of residual surfactants after the post-synthetic modification process, that allows nDUT-5:Ln^{3+} and nMOF-253:Ln^{3+} to form stable and homogeneous dispersions with slightly increased particle sizes, due to a swelling of the crystal structure and less coverage by surfactants.

Photophysical properties

The evaluation of the photophysical properties of bulk MOFs and nMOFs was accomplished by comparing the obtained results of qualitative PL spectra, overall luminescence decay times τ, QYs and linker triplet state energy determinations, as well as UV-Vis-DRS.

Comparison of the photophysical properties of the investigated bulk MOFs and nMOFs. PL spectra were recorded for all Ln^{3+}-containing MOFs and nMOFs, with $Ln^{3+} = Eu^{3+}$, Tb^{3+} (see Fig. 6 for excitation and emission spectra). For excitation, a broad band at 280–350 nm appears in the excitation spectra of all investigated MOFs and nMOFs at similar wavelengths and with similar band shapes that represent the $\pi^* \leftarrow \pi$ excitation of the linkers. Subsequently, the excited π-electrons of the linker undergo an intersystem crossing to a triplet state followed by an energy transfer to excited 4f-states of the trivalent lanthanides – this describes the so-called 'antenna effect'. Other obvious features in the excitation spectra shown in Fig. 6 are direct excitations of Ln^{3+} that are prominent for Eu^{3+}-bdc and nEu^{3+}-bdc (Eu^{3+}: $^5D_{1,2,4}$, $^5L_6 \leftarrow {}^7F_0$ and $^5D_{1,3,4} \leftarrow {}^7F_1$ at 525 nm, 464 nm, 392 nm, 361 nm and 533 nm, 414 nm, 379 nm, respectively) and weak to hardly observable in the excitation spectra of Tb^{3+}-bdc and nTb^{3+}-bdc (Tb^{3+}: $^5D_2 \leftarrow {}^7F_6$, $^5L_{10} \leftarrow {}^7F_6$, $^5D_3 \leftarrow {}^7F_6$ and $^5D_4 \leftarrow {}^7F_6$ at 351 nm, 368 nm, 376 nm and 489 nm, respectively). Although quantum mechanically unfavoured, these peaks demonstrate the weak receptivity of these Ln^{3+}-MOFs to absorb light in a direct way without participation of the linker, indicating the preferred route of an excitation *via* a sensitizer linker, as the broad $\pi^* \leftarrow \pi$ excitations of the linkers surpass the direct excitations of the investigated Ln^{3+}-MOFs in terms of intensity.

The emission spectra of the investigated Eu^{3+}-containing MOFs and nMOFs show the typical Eu^{3+} transitions $^5D_0 \rightarrow {}^7F_0$, $^5D_0 \rightarrow {}^7F_1$, $^5D_0 \rightarrow {}^7F_2$, $^5D_0 \rightarrow {}^7F_3$, $^5D_0 \rightarrow {}^7F_4$, $^5D_0 \rightarrow {}^7F_5$ and $^5D_0 \rightarrow {}^7F_6$, which correspond to the emission signals at 580 nm, 593 nm, 616 nm, 652 nm, 700 nm, 753 nm, and 810 nm, respectively. The emission bands differ in terms of relative intensity and shape. For instance, the coordinated Eu^{3+} in Eu^{3+}-bdc and nEu^{3+}-bdc causes a splitting of the $^5D_0 \rightarrow {}^7F_2$ and $^5D_0 \rightarrow {}^7F_4$ transitions, while Eu^{3+} inside the pores of DUT-5:Eu^{3+} and MOF-253:Eu^{3+} gives broader, single-maxima emission bands. This signal broadening is indicative for multiple, different local electric fields of Eu^{3+} in the pores or on the MOF surface, which differs from the distinct crystallographic Ln^{3+}-positions in Ln^{3+}-bdc and nLn^{3+}-bdc. For the post-synthetic modification, the MOF pores allow for multiple locations inside the pores for Eu^{3+}. In addition, the relative intensities of $^5D_0 \rightarrow {}^7F_2$ and $^5D_0 \rightarrow {}^7F_4$ vary between DUT-5:Eu^{3+} and MOF-253:Eu^{3+}, depending on the specific Eu^{3+} position within the crystal structure. Both effects are well known in the literature[56] and provide evidence for different electrostatic environments for Eu^{3+} inside the pores. Furthermore, the asymmetry ratio of Eu^{3+} provides valuable insights concerning its local environment and is defined as the ratio of the integrated intensities $I(^5D_0 \rightarrow {}^7F_2)$ and $I(^5D_0 \rightarrow {}^7F_1)$. As the $^5D_0 \rightarrow {}^7F_1$ transition is predominantly unaffected by the local environment,[57] a low asymmetry ratio indicates minimal distortions in the electric field, with $^5D_0 \rightarrow {}^7F_2$ being comparatively weaker and Eu^{3+} is located at distinct positions. However, when the distortion in the electrostatic environment of Eu^{3+} increases, *i.e.* Eu^{3+} is located at positions with different local environments, the intensity of the $^5D_0 \rightarrow {}^7F_2$ transition also increases, resulting in a higher asymmetry ratio. The calculated asymmetry ratios for bulk Eu^{3+}-bdc and nEu^{3+}-bdc are 5.07 and 6.57, respectively. This observation supports the assertion that surfactants remain present in the pores and/or at the surface of nEu^{3+}-bdc after the washing procedure, leading to distortion of the local environment of Eu^{3+}. The post-synthetically modified MOF-253:Eu^{3+} and nMOF-253:Eu^{3+} also following the described trend indicative by the asymmetry ratios 4.47 and 6.49, respectively. Additionally, in the case of the post-synthetically modified MOFs, the higher average diffusion pathway affords improved pore occupancy of Eu^{3+}, resulting in even more different electrostatic environments than in Ln^{3+}-bdc. Asymmetry ratios of 6.34 and 6.35 are observed for DUT-5:Eu^{3+} and nDUT-5:Eu^{3+}, respectively. These ratios indicate a more distorted local environment for Eu^{3+} in DUT-5:Eu^{3+} compared to

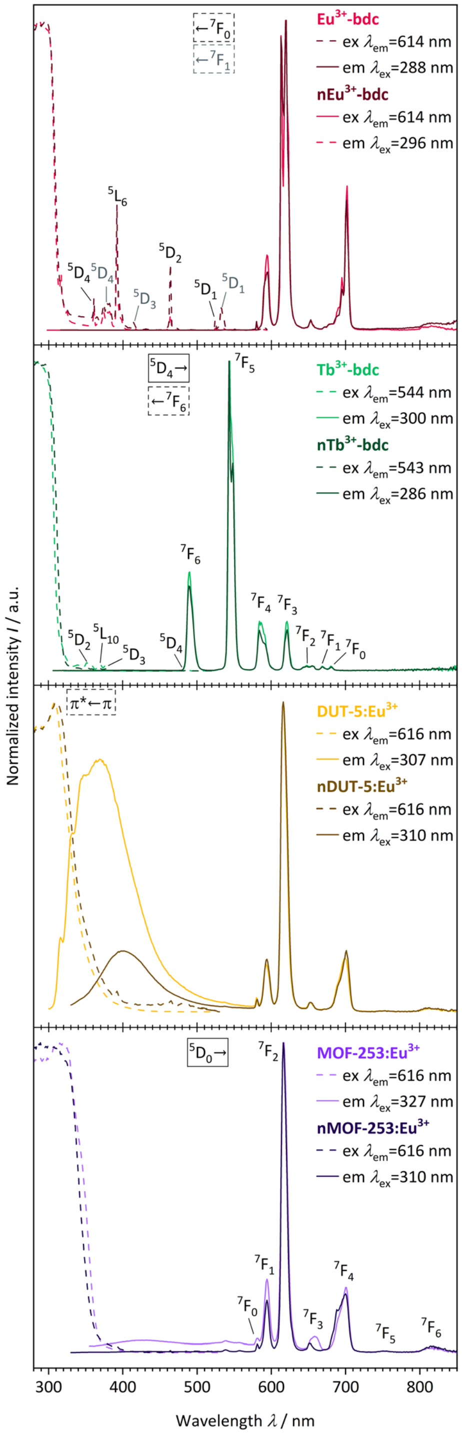

Fig. 6 Qualitative PL excitation and emission spectra of Eu^{3+}-bdc (pale red), nEu^{3+}-bdc (dark red), Tb^{3+}-bdc (pale green), nTb^{3+}-bdc (dark green), DUT-5:Eu^{3+} (pale yellow), nDUT-5:Eu^{3+} (dark yellow), MOF-253:Eu^{3+} (pale violet) and nMOF-253:Eu^{3+} (dark violet). Electronic states are exemplarily denoted for clarity with the corresponding electronic transitions for the linker, Eu^{3+} and Tb^{3+}, respectively.[56,58]

MOF-253:Eu^{3+} and Eu^{3+}-bdc, while the environment of Eu^{3+} in nDUT-5:Eu^{3+} is similar to other nMOF-253:Eu^{3+} and Eu^{3+}-bdc.

The emission spectra of Tb^{3+}-bdc and nTb^{3+}-bdc exhibit the typical emission pattern of Tb^{3+} with the transitions $^5D_4 \rightarrow {}^7F_6$, $^5D_4 \rightarrow {}^7F_5$, $^5D_4 \rightarrow {}^7F_4$, $^5D_4 \rightarrow {}^7F_3$,$^5D_4 \rightarrow {}^7F_2$, $^5D_4 \rightarrow {}^7F_1$ and $^5D_4 \rightarrow {}^7F_0$, which can be attributed to sharp bands at 489 nm, 543 nm, 584 nm, 621 nm, 647 nm, 669 nm, and 680 nm, respectively.[58] Tb^{3+} does not show emission in post-synthetically modified DUT-5:Tb^{3+}, nDUT-5:Tb^{3+}, MOF-253:Tb^{3+} and nMOF-253:Tb^{3+} since the sensitization of Tb^{3+} by the energy transfer from the linkers to Tb^{3+} is not preferred (Fig. SI21 and 22†). In order to investigate the reasons for the neglectable energy transfer, the donor triplet state energies of the linkers were determined and subsequently compared with the emitting energy state level $^5D_4$ of Tb^{3+} in terms of energy. Latva *et al.*[59] state that donor–acceptor energy states should be optimally separated by 2000–4000 cm^{-1}. The emitting state $^5D_4$ of Tb^{3+} is located at 20 470 cm^{-1},[60] whereas the donor triplet states of Tb^{3+}-bdc, DUT-5 and MOF-253 are located at 24 691 cm^{-1}, 21 079 cm^{-1} and 20 877 cm^{-1}, respectively (Fig. SI23–25†). Since the energy states for DUT-5 and MOF-253 are energetically too close to the Tb^{3+} energy state $^5D_4$, high energy back-transfer rates dominate the systems, and therefore no Tb^{3+}-based emissions are observed. In contrast, Eu^{3+} has two energetic states $^5D_{1,2}$ at 19 026 cm^{-1} and 21 499 cm^{-1}, respectively, which get addressed to as acceptor states[61] for the sensitization energy transfer from the linker to Eu^{3+} and is in accordance with Latva's rule.

Altogether, the comparison of Ln^{3+}-containing MOFs and nMOFs show a benefit of nanoscale particles regarding the sensitizing efficiency as indicated by a strong decrease in the intensity of the linker-based emission bands.

The previously described emission processes were further characterised by performing luminescence overall decay time measurements to determine lifetimes τ (Fig. SI26–31†), with the results being given in Table 2. Lifetimes of the emitting states in millisecond range indicate quantum mechanically unfavoured phosphorescent emission processes caused by parity forbidden 4f–4f transitions of the Ln^{3+} ions. Typical lifetimes for phosphorescence processes are 0.9055(6) ms for Eu^{3+}-bdc or 0.701(4) ms for nEu^{3+}-bdc, for instance. However, for the non-Ln^{3+}-containing MOFs, lifetimes in nanosecond range were recorded and are indicative for fluorescence processes of the linker-based emission with 2.49(6) ns for DUT-5 or 3.6(1) ns for nDUT-5, for instance.

In fact, an important aspect when considering the efficiency of the emission of the Ln^{3+}-MOFs is its residual linker-based emission intensity. The presence and intensity of the emission band of the linker is a reciprocal indicator for the efficiency of the sensitizing effect. The better the energy transfer from the linker to Ln^{3+}, the lower the emission band intensity of the linker. This energy transfer is strongly depending on the donor–acceptor distance *i.e.*, linker and Ln^{3+}. As nDUT-5:Ln^{3+} and nMOF-253:Ln^{3+} are smaller in size than their bulk analogues, the average Ln^{3+} diffusion pathway becomes shorter, and a better pore occupancy can be achieved. Accordingly, the linker-based emission intensity in the emission spectrum of nDUT-5:Eu^{3+} at 400 nm is lower than the bulk analogue. This is in corroboration with a decreased linker-based QY from 10.4(3)% to 4.5(3)% for DUT-5:Eu^{3+} and nDUT-5Eu^{3+}, respectively. The linker-based emission band of nMOF-253:Eu^{3+} yet diminishes completely. Both reveal nicely the advantages of nanoparticles. Interestingly, although the MOF-253, nMOF-253, MOF-253:Tb^{3+} and nMOF-253:Tb^{3+} show linker-based emission bands in their PL spectra QYs are <1%, which, however, is consistent with the low emission intensities observed with the naked eye (Fig. 7). This is also evidence for energy release by rather non-radiative processes than light emission. Moreover, the undoped DUT-5 and nDUT-5 show linker-based QYs of 5.1(5)% and 14.8(6)%, respectively, which is in accordance with the observed higher intensity of nDUT-5 compared to its bulk analogue, accompanied by a bathochromic shift as explained later in more detail. On the other hand, Ln^{3+}-bdc and nLn^{3+}-bdc do not show any linker-based emission bands at all, which confirms a highly efficient energy transfer. This results in excellent Ln^{3+}-based QYs as the ratio of emitted to absorbed photons of 94(2)% and 78.1(3)% for Tb^{3+}-bdc and nTb^{3+}-bdc, respectively (see Table 2). The respective Ln^{3+}-based QYs of 33(2)% for Eu^{3+}-bdc and 23.7(3)% for nEu^{3+}-bdc are lower than the Ln^{3+}-based QYs of their Tb^{3+}-analogues indicating a better energetical match between the excited states of the sensitizer for Tb^{3+}. Different to Ln^{3+}-coordination sites of these MOFs, post-synthetically modified MOF:Ln^{3+}s show lower Ln^{3+}-QYs as the Ln^{3+}-to-linker distances increase (Ln^{3+}-based QY of 2.0(1)% for MOF-253:Eu^{3+}, for instance). As discussed early, DUT-5:Tb^{3+} and nDUT-5:Tb^{3+} do not show Tb^{3+}-based emission due to the mismatch of Tb^{3+}-linker energy states while the linker-based QYs also decreasing from 11.5(3)% to 4.6(2)% from DUT-5:Tb^{3+} to nDUT-5:Tb^{3+}. For nDUT-5:Eu^{3+}, however, the Ln^{3+}-based QY can exceed the bulk MOF (Ln^{3+}-based QYs: 3.6(1)% compared to 2.1(2)%) corroborated by a longer lifetime τ (see Table 2). Accordingly, a decreased Ln^{3+}-based QY may be concluded as a result of the surfactant influence, although there is no general trend.

In addition, light absorption was investigated by UV-Vis-DRS. In general, it reveals broad absorption from 200–320 nm for all investigated MOFs, which can be assigned to the $\pi^* \leftarrow \pi$ transition of the linkers and fits nicely the excitation spectra seen in Fig. 6. However, all absorption spectra of the investigated nMOFs show this broad absorption band starting at 200 nm but instead of tailing at 320 nm, the absorption band shows tailing up to 700 nm for nTb^{3+}-bdc, for instance, which implies a contribution of further absorption processes along with the $\pi^* \leftarrow \pi$ transition. The range of this multiple-process absorption band varies with each investigated MOF and is displayed in Fig. SI17–20.† Since this broader absorption band appears exclusively in investigated nMOF absorption spectra, the absorption band is attributed to the surfactants CTAB and PVP$_{40\,000}$. Therefore, the investigated nMOFs appear yellow at daylight compared to their colourless bulk analogues (Fig. 7 and SI33† as well as a video download). In addition, only Eu^{3+}-bdc and nEu^{3+}-bdc spectra show low-intensity, sharp absorption peaks at 395 nm, 466 nm and 535 nm which can again be assigned to the respective 4f–4f transitions $^5L_6 \leftarrow {}^7F_0$, $^5D_2 \leftarrow$

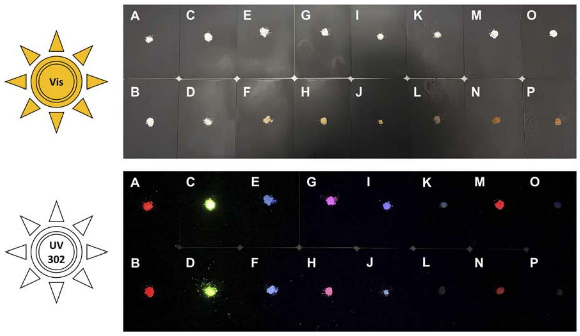

Fig. 7 Photographs of powders of investigated bulk MOFs and nMOFs exposed to Vis-light (top) and UV-light (302 nm, bottom). A = Eu^{3+}-bdc, B = nEu^{3+}-bdc, C = Tb^{3+}-bdc, D = nTb^{3+}-bdc, E = DUT-5, F = nDUT-5, G = DUT-5:Eu^{3+}, H = nDUT-5:Eu^{3+}, I = DUT-5:Tb^{3+}, J = nDUT-5:Tb^{3+}, K = MOF-253, L = nMOF-253, M = MOF-253:Eu^{3+}, N = nMOF-253:Eu^{3+}, O = MOF-253:Tb^{3+}, P = nMOF-253:Tb^{3+}.

$^7F_1$ and $^5D_1 \leftarrow {}^7F_1$ already observed in the excitation spectra of Eu^{3+}-bdc and nEu^{3+}-bdc.

Comparison of the chromaticity of investigated bulk MOFs and nMOFs. The contributions of linker-based emission and Ln^{3+}-based emission to the overall light emission as a specific colour by each MOF is shown in a chromaticity diagram according to CIE 1931 (Fig. 8). It was calculated from the PL data of all bulk MOFs and nMOFs investigated and clearly shows the effect of an improved energy transfer from the linker to Ln^{3+} in nMOFs compared to bulk MOFs. This corroborates the observed emission spectra and results in an emission colour shift. In general, the emission of nEu^{3+}-bdc and nTb^{3+}-bdc is less influenced by the nano-character of the particles than the emission of the post-synthetically modified nDUT:Ln^{3+} and nMOF-253:Ln^{3+}. Both, nDUT-5 and nMOF-253 show shifted overall luminescence but to opposing wavelength regions. *E.g.*, the emission band of nDUT-5 is shifted by 18 nm from 377 nm to 395 nm compared to DUT-5. In contrast, nMOF-253 does not show the additional emission band of MOF-253, as explained earlier, which shifts the chromaticity towards green. This means that a combination of the processes of all MOF components, post-synthetic modification and the surfactants influence the overall luminescence and its chromaticity. An overview is given in Fig. 7 and SI33,† as well as a video download.

Conclusion

This work presents new aspects of the impact of nanoparticle formation on morphological and photophysical properties compared to the bulk archetype MOFs for Ln^{3+}-MOFs and archetype MOFs doped post-synthetically modified by impregnation with lanthanide ions, shown for Ln^{3+}-bdc, DUT-5:Ln^{3+} and MOF-253:Ln^{3+} ($Ln^{3+} = Eu^{3+}$, Tb^{3+}). Nanoscale variants of the three archetype MOFs have been successfully achieved by surfactant-assisted bottom-up synthesis as fully-characterised nMOFs.

The nMOFs were synthesized with particle sizes down to 35 nm as nDUT-5 demonstrates (21-times smaller than DUT-5). Consequently, a particle consists of only a couple unit cells of the 3D framework. Furthermore, particle size distributions were tremendously narrowed down to ≈1% of their original bulk particle size distribution and stabilized in dispersion by $PVP_{40\,000}$ and CTAB. After post-synthetic modification, the nMOFs:Ln^{3+} benefit from residual surfactants as good as non-post-synthetically modified nMOFs in terms of dispersibility and particle size. The shorter average free path of the diffusion of Ln^{3+} in nMOF:Ln^{3+} leads to a better pore occupancy and an improved energy transfer from the linker to the Ln^{3+}. The importance of suitable energy differences of the excited states of the MOFs and incorporated Ln^{3+}-ions becomes evident for the non-preferred sensitization of Tb^{3+} in nMOF:Tb^{3+} combinations. In contrast, MOFs and nMOFs with Ln^{3+} as connectivity centres show higher QYs up to 94% and 78% for Tb^{3+}-bdc and nTb^{3+}-bdc, as an energy transfer *via* the electronic system of the MOF is available. This results in chromaticity shifts between MOFs and nMOFs being either bathochromic or hypsochromic.

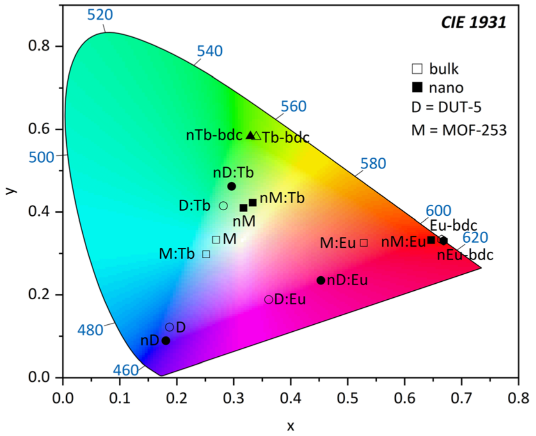

Fig. 8 Chromaticity diagram according to CIE 1931 calculated from PL data of Ln^{3+}-bdc, nLn^{3+}-bdc, DUT-5, nDUT-5, MOF-253, nMOF-253, DUT-5:Ln^{3+}, nDUT-5:Ln^{3+}, MOF-253:Ln^{3+} and nMOF-253:Ln^{3+} (Ln^{3+} = Eu^{3+}, Tb^{3+}) investigated in this work. Hexagon = Eu^{3+}-bdc; triangle = Tb^{3+}-bdc; square = MOF-253 and MOF-253:Ln^{3+}; circle = DUT-5 and DUT-5:Ln^{3+}; D = DUT-5; and M = MOF-253. Empty symbols represent bulk MOFs, while filled symbols represent nMOFs.

Altogether, this work provides insights into the photophysical and morphological properties of nano-sized lanthanide-containing MOFs, the pros and cons associated with the usage of surfactants as well as two different ways of functionalizing of these versatile three-dimensional compounds. We demonstrate, how the synthesis of nMOFs can be controlled by reagents such as surfactants, how the light emission of Ln^{3+}-containing MOFs can be influenced either by changing the size and morphology of the particles or by incorporate the lanthanide at different stages of the synthesis process (early in the synthesis procedure or post-synthetic), as well as how the choice of IBU-linker-Ln^{3+} combination affects the energy transfer efficiency and luminescence efficiency.

Experimental

All chemicals were used as purchased without further purification. The rare-earth nitrates $Ln(NO_3)_3 \cdot 6H_2O$ (Ln = Eu, Tb, Gd;

99.9% pur.); the organic linkers benzene-1,4-dicarboxylic acid (H_2bdc, 98% pur.), biphenyl-4,4′-dicarboxylic acid (H_2bpdc, 97% pur.) and 2,2′-bipyridine-5,5′-dicarboxylic acid (H_2bpydc, 97% pur.); and the aluminium salt $AlCl_3 \cdot 6H_2O$ (99% pur.) have been supplied from abcr. In addition, the aluminium salts $Al(NO_3)_3 \cdot 9H_2O$ (≥98% ACS gra.); the surfactants *N*,*N*,*N*-trimethylhexadecan-1-ammonium bromide (CTAB, ≥96% pur.) and 1-ethenylpyrrolidin-2-one ($PVP_{40\,000}$, avg. mol. wt. 40 000, MQ: 200); and the reference material polytetrafluoroethylene (PTFE, 1 μm particle size) and magnesium oxide (MgO, MQ: 300) were purchased from Sigma-Aldrich (Merck). Moreover, the solvents *N*,*N*-dimethylformamide (DMF, 99% pur., purchased from Grüssing), ethanenitrile (MeCN, ≥99.8% pur., purchased from Chemsolute (Th. Geyer)), ethanol (EtOH, ≥99.8% abs., Fischer Scientific) and triethylamine (TEA, 99% pur., Fischer Scientific) did not undergo any additional drying process. Nitric acid (HNO_3, tech. qual.) was purchased from STOCKMEIER Chemie. Furthermore, only demineralized water (H_2O) was used for synthesis, analysis, and product purification processes.

Synthesis and post-synthetic modification procedure

Synthesis of Eu^{3+}-bdc and Tb^{3+}-bdc. The synthesis according to Guo *et al.*[43] was modified in certain steps and started by mixing of 80 mg (0.179 mmol) $Eu(NO_3)_3 \cdot 6H_2O$ or 80 mg (0.177 mmol) $Tb(NO_3)_3 \cdot 6H_2O$, respectively, and 32 mg (0.193 mmol) H_2bdc inside a 30 mL snap-on cap glass vial. Subsequent dilution in 20 mL DMF, 4 mL abs. EtOH and 4 mL H_2O resulted in a colourless, transparent solution. After the addition of four drops of TEA, the solution became opaque. After shaking for 60 s, five drops of 6 M HNO_3 were added until the dispersion became transparent again. The vial was closed with a lid, sealed with Parafilm® and placed in an autoclave (Heraeus) at 55 °C for 7 d. Finally, the colourless precipitate was washed stepwise with 10 mL of DMF and EtOH, consecutively, and centrifuged at 10 565 g (rcf) for 10 min after each step.

Eu^{3+}-bdc. Drying under vacuum gave 38 mg (0.026 mmol, 1472.72 g mol^{-1}, 15%) of a colourless powder. Organic elemental analysis ($^3_\infty[Eu_3(bdc)_{4.5}] \cdot 3.3DMF \cdot 0.9H_2O$, found: C, 37.9; H, 3.0; N, 3.2. Calc. for $Eu_3C_{45.9}H_{42.9}N_{3.3}O_{22.2}$: C, 37.4; H, 2.9; N, 3.1%).

Tb^{3+}-bdc. Drying under vacuum gave 48 mg (0.032 mmol, 1510.96 g mol^{-1}, 18%) of a colourless powder. Organic elemental analysis ($^3_\infty[Tb_3(bdc)_{4.5}] \cdot 3.7DMF \cdot 1.4H_2O$, found: C, 37.4; H, 3.0; N, 3.5. Calc. for $Tb_3C_{47.1}H_{46.7}N_{3.7}O_{23.1}$: C, 37.4; H, 3.1; N, 3.4%).

Synthesis of nEu^{3+}-bdc and nTb^{3+}-bdc. The synthesis according to Neufeld *et al.*[46] was modified in certain steps and started by dissolving 280 mg (0.628 mmol) $Eu(NO_3)_3 \cdot 6H_2O$ or 280 mg (0.618 mmol) $Tb(NO_3)_3 \cdot 6H_2O$, respectively, and 4220 mg (29.90 mmol) $PVP_{40\,000}$, separately, in 40 mL DMF under vigorous stirring. Subsequently, 190 mg (1.14 mmol) H_2bdc and 3220 mg (8.78 mmol) CTAB were dissolved in 200 mL DMF inside a 500 mL three-necked round-bottomed flask equipped with a reflux condenser, under vigorous stirring at 55 °C for 60 min. Afterwards, the previously prepared solutions were then gradually added, followed by the addition of 200 μL of TEA. The reaction mixture became slightly opaque and was stirred vigorously for a further 60 min at 55 °C. Further heating at 90 °C for 6 h resulted in a thick opaque, pale yellowish dispersion, which was washed with 10 mL DMF (1×) and 10 mL EtOH (2×), consecutively, and centrifuged at 17 855 g (rcf) for 10 min after each step.

nEu^{3+}-bdc. Drying under vacuum gave 188 mg of a pale yellowish powder.

nTb^{3+}-bdc. Drying under vacuum gave 121 mg of a pale yellowish powder.

Synthesis of DUT-5. The synthesis according to Senkovska *et al.*[44] started by suspending 521 mg (2.15 mmol) H_2bpdc in 15 mL DMF and stirring at 55 °C for 30 min. Then, 1042 mg (2.778 mmol) $Al(NO_3)_3 \cdot 9H_2O$ were added and dissolved. The reaction mixture was kept in a closed 120 mL pressure tube (Ace Glass) for 24 h at 120 °C. Subsequent liquid/solid separation by centrifugation (6762 g (rcf), 10 min) yielded a colourless solid. Final drying under vacuum gave 946 mg (1.923 mmol, 492.05 g mol^{-1}, 89%) of a colourless powder. Organic elemental analysis ($^3_\infty[Al(OH)bpdc] \cdot 2.4DMF \cdot 1.8H_2O$, found: C, 51.8; H, 5.5; N, 6.8. Calc. for $AlC_{21.1}H_{29.4}N_{2.4}O_{9.2}$ C, 51.6; H, 6.0; N, 6.8%).

Synthesis of nDUT-5. The synthesis according to Neufeld *et al.*[46] was modified in certain steps and started with the dissolution of 392 mg (1.62 mmol) H_2bpdc and 2250 mg (6.174 mmol) CTAB in 200 mL DMF at 55 °C. At the same time, 1051 mg (6.174 mmol) $PVP_{40\,000}$ and 417 mg (1.11 mmol) $Al(NO_3)_3 \cdot 9H_2O$ were dissolved in 40 mL and 20 mL DMF, respectively, and gradually added to the reaction mixture. After 5 min of stirring, adding of 300 μL of TEA made the solution opaque. This was followed by a further 1 h of stirring at 55 °C. Afterwards, the reaction mixture was treated at 120 °C for 24 h in a reflux apparatus. First, the purification process was started by separating the precipitate by centrifugation at 17 855 g (rcf) for 10 min. Second, washing with 15 mL DMF (4×) and 10 mL H_2O (4×), followed by the above-mentioned centrifugation procedure after each step, yielded a pale brownish residue. Finally, the specimen was dried under vacuum to give 467 mg of a pale brownish powder.

Synthesis of MOF-253. The synthesis according to Bloch *et al.*[45] was modified in certain steps and started by suspending 306 mg (1.25 mmol) H_2bpydc in 30 mL DMF and stirring at 55 °C for 30 min. After dissolving 303 mg (1.26 mmol) $AlCl_3 \cdot 6H_2O$, the reaction mixture was heated for 24 h at 120 °C in a closed pressure tube (Ace Glass). The pale greenish precipitate was centrifuged (10 565 g (rcf), 10 min) and subsequently reheated for 15 min in 20 mL DMF under reflux for purification. After a short cooling period, the product was centrifuged again (1690 g (rcf), 10 min) and the supernatant removed. Repeated purification with 20 mL DMF (1×) and 20 mL EtOH (2×), followed by vacuum drying yielded 324 mg (0.852 mmol, 380.29 g mol^{-1}, 68%) of a colourless powder. Organic elemental analysis ($^3_\infty[Al(OH)bpydc] \cdot 1.3EtOH \cdot 1.9H2O$, found: C, 46.1; H, 4.9; N, 7.4. Calc. for $AlC_{14.6}H_{18.6}N_2O_{8.2}$: C, 46.1; H, 5.0; N, 7.4%).

Synthesis of nMOF-253. The synthesis according to Neufeld *et al.*[46] was modified in certain steps and started by dissolving of 159 mg (0.651 mmol) H_2bpydc and 899 mg (2.47 mmol) CTAB in 80 mL DMF at 55 °C. Simultaneously, 421 mg (2.98 mmol) PVP_{40}

$_{000}$ were dissolved in 16 mL DMF and gradually added to the reaction mixture. Additionally, 108 mg (0.447 mmol) $AlCl_3 \cdot 6H_2O$ were added as solid. After 5 min of stirring, adding of 120 μL of TEA made the solution opaque. This was followed by another 1 h of stirring at 55 °C. Afterwards, the reaction mixture was treated at 120 °C for 24 h in a reflux apparatus. First, the purification process was started by separating the precipitate by centrifugation at 17 855 g (rcf) for 10 min. Second, washing with 10 mL DMF (4×) and 10 mL EtOH (4×), followed by the aforementioned centrifugation procedure after each step, yielded in a dark brownish residue. Finally, the specimen was dried under vacuum, yielding 136 mg of a dark brownish powder.

Post-synthetic modification of DUT-5, nDUT-5, MOF-253 and nMOF-253. Two different approaches going to be stated in the following section. For post-synthetic modification, different amounts of $Eu(NO_3)_3 \cdot 6H_2O$ and $Tb(NO_3)_3 \cdot 6H_2O$ were used in combination with different temperatures and solvents to yield DUT-5:Ln^{3+}, nDUT-5:Ln^{3+}, MOF-253:Ln^{3+} and nMOF-253:Ln^{3+}.

The first post-synthetic modification approach was carried out at room temperature (RT) in a snap-on cap glass vial. Previously, $Ln(NO_3)_3 \cdot 6H_2O$ has been dissolved in EtOH. Then, 40 mg specimen were soaked with 1 mL of a 0.1 M Ln^{3+}-solution. After 5 min of sonicating, the vial was closed and left untouched for one week. After rinsing the specimen out of the vial, it was centrifuged at 17 855 g (rcf) for 10 min. Ultimately, the post-synthetically modified sample was washed with 2 mL of EtOH, centrifuged and dried under vacuum to obtain a powder.

The second post-synthetic modification approach was carried out at 65 °C in a closed pressure tube (Ace Glass) according to the procedure of Lu *et al.*,[62] with some modifications. Previously, 45 mg $Ln(NO_3)_3 \cdot 6H_2O$ were dissolved in 10 mL MeCN (0.01 M). After adding 40 mg MOF to the mixture, the mixture was again dispersed with 5 mL MeCN and sonicated for 5 min. This was followed by a heating step for 24 h and the final purification process, consisting of centrifugation (17 855 g (rcf), 10 min), washing (10 mL MeCN) and sonication (5 min) three times consecutively. After drying under vacuum, the post-synthetically modified sample was obtained as powder.

Analytical methods

Powder X-ray diffraction (PXRD). Structural information has been acquired using a X'Pert Pro MPD with Data Collector (ver. 5.4.0.90) software from PANalytical. The X-ray beam was generated by an Empyrean Cu LFF X-ray tube ($\lambda_{\text{Cu-K}\alpha} = 154.06$ pm) at 40 kV and 40 mA. After focusing the incident beam by Soller slits (0.04 rad), a beam mask (10 mm) and a fixed anti-scatter slit (1°), a flattened sample presented on a silicon waver diffracted the beam, which then passed through an angled anti-scatter slit (0.5°), again Soller slits (0.04 rad) and a Beta-filter Nickel towards an X'Celerator with a FASS detector. The measurement was performed in Bragg–Brentano geometry between 3.5° and 60° in 2θ on account of a PW3050/60 goniometer at RT and ambient atmosphere. Finally, the diffractogram was background corrected using DIFFRAC.EVA (ver. 5.2.0.5, Bruker) and plotted using OriginPro 2023 (ver. 10.0.0.154, OriginLab).

Dynamic light scattering (DLS). Particle size and its distribution were determined using a StabiSizer® PMX 200CS from Particle Metrix. The Microtrac FLEX Application Software (ver. 10.5.4.) from Mictrotrac was used for data acquisition. The sample preparation began by rinsing and filling up to half of the volume of the snap-on cap glass vials with EtOH. Subsequently, a spatula tip of sample was added to one of the vials and sonicated for 10 min at 30 °C. After checking the stability of the dispersion, data acquisition was performed, first for the blank (EtOH only) and then for the dispersion. Additionally, for improving statistics, the measurement was carried out three times, for 120 s each. The particle size distribution plots shown in this work represent the average of these three measurements and have been plotted using OriginPro 2023 (ver. 10.0.0.154, OriginLab). Furthermore, the average value for particle size is denoted with $\pm 2\sigma$.

Scanning electron microscopy (SEM). Particle morphology was examined using a GeminiSEM 560 and the software SMART SEM (ver. 6.08) from Carl Zeiss NTS. Ground samples were waved onto a sticky carbon pad attached to an aluminium carrier. The surface was cleaned by carefully blowing off loose material with pressurized air, to ensure no contamination within the vacuum chamber of the instrument. The electron images were recorded with a 7.5 μm aperture and an acceleration voltage of 3 kV at a working distance of 3 mm using a Schottky field emitter as electron source. Moreover, a SE-InLens detector afforded the images from secondary electrons. Particle sizes were determined using ImageJ (ver. 1.53f51) from National Institute of Health.

Microwave plasma–atomic emission spectroscopy (MP-AES). The amounts of Eu^{3+} and Tb^{3+} in the samples were determined by a 4210 MP-AES with MP Expert Software (ver. 1.6.0.9255) from Agilent Technologies using the external calibration method. Standard solutions for Al (22102, Grüssing), Eu (2414.1, Carl Roth) and Tb (2476.1, Carl Roth) were diluted to give standard solutions of 0.05 mg L^{-1}, 0.10 mg L^{-1}, 0.50 mg L^{-1}, 1.00 mg L^{-1}, 5.00 mg L^{-1} and 10.00 mg L^{-1} for external calibration. First, the sample was dissolved in HNO_3 (wt 1%). For DUT-5:Ln^{3+}, nDUT-5:Ln^{3+}, MOF-253:Ln^{3+} and nMOF-253:Ln^{3+}, the sample did not dissolve completely, so that an additional step of centrifugation (20 707 g (rcf), 15 min) was carried out to remove the linker (stem solution). Subsequently, the procedure was the same to all MOFs. Several dilutions were prepared from stem solution to theoretically match the concentration range of the external calibration. Intensity was recorded at characteristic atomic emission wavelengths (Al: 394.401 nm, 396.152 nm; Eu: 381.967 nm, 412.973 nm; Tb: 350.917 nm, 384.874 nm) were used to determine the concentration of the analytes. The instrument required 90 min for sample uptake, followed by 30 min for rinsing and 15 min for flow stabilization. This procedure was repeated after each dilution.

UV-Vis diffuse reflectance spectroscopy (UV-Vis-DRS). Diffuse reflectance spectra were acquired using a Cary 5000 UV-Vis-NIR spectrophotometer and the Cary WinUV Scan Application software (ver. 6.3.0.1595) from Agilent Technologies. The instrument was equipped with a Praying Mantis™ Diffuse Reflectance Accessory from Harrick Scientific Products and operated in double beam mode with reduced slit height. Raw data is given in reflectance units. Since this is a relative method, PTFE was chosen as reference material. Both, reference and MOF were ground and successively filled into a DRP-SAP microsample-cup (Harrick Scientific Products) and flattened with a spatula. Finally, the reflectance spectrum was recorded and corrected by PTFE according to the following operation: $\%R_{\mathrm{corr}}^{\mathrm{MOF}} = \%R_{\mathrm{raw}}^{\mathrm{MOF}}/\%R_{\mathrm{raw}}^{\mathrm{PTFE}}$.

Photophysical methods for the determination of qualitative and quantitative properties. Qualitative PL excitation and emission spectra were recorded using a Jobin Yvon Fluorolog 3 with the FluorEssence™ for Windows® (ver. 3.9.0.1) software supplied by HORIBA. A Xe short-arc lamp (USHIO) was used in conjunction with a double-grated monochromator at the excitation site, while another monochromator was used in conjunction with a photomultiplier tube R928P (HAMAMATSU PHOTONICS K.K.) at the emission site to record the spectra. Additionally, mathematical corrections for monochromators and detectors were provided by the manufacturer. The spectral distribution of the lamp is measured by a reference detector (R signal) and corrected *in situ*. For measurement, the sample was filled into a cylindric synthetic-quartz glass cuvette (proQuarz) and positioned in the focus point of the beam. To acquire a full spectrum, a long-pass edge filter 550 (Newport) was placed in the beam path between the sample and the detector. The excitation and emission spectra were recorded separately and then plotted together in one graph with OriginPro 2023 (ver. 10.0.0.154) from OriginLab.

QY determination was performed using a Jobin Yvon Fluorolog 3 with the FluorEssence™ for Windows® (ver. 3.9.0.1) software equipped with a Quanta-φ Integrating Sphere F-3029 from HORIBA. For the measurement, the reference and sample, respectively, were filled into a micro cell cuvette 18-F/ST/C/Q/10 from Starna Scientific. The quantum yield determination was repeated three times for each specimen and related to the reference material MgO. An additional check using another standard material γ-[$\mathrm{Tb_4(OAc)_{12}(ptpy)_2}$] verified the calibration of the Quanta-φ Integrating Sphere ($\lambda_{\mathrm{ex}} = 310$ nm, $\lambda_{\mathrm{em}} = 450$–$700$ nm; $\Phi_{\mathrm{exp}} = 46(1)\%$, $\Phi_{\mathrm{lit}} = 46(3)\%$ (ref. 63)). $\mathrm{Ln^{3+}}$-based QYs were determined with $\lambda_{\mathrm{ex}} = 310$ nm and $\lambda_{\mathrm{em}} = 450$–$700$ nm. Linker-based QYs were determined with $\lambda_{\mathrm{ex}} = 310$ nm, $\lambda_{\mathrm{em}} = 315$–$520$ nm for DUT-5; $\lambda_{\mathrm{ex}} = 310$ nm, $\lambda_{\mathrm{em}} = 335$–$570$ nm for nDUT-5; $\lambda_{\mathrm{ex}} = 310$ nm, $\lambda_{\mathrm{em}} = 330$–$540$ nm for DUT-5:$\mathrm{Tb^{3+}}$ and nDUT-5:$\mathrm{Tb^{3+}}$; $\lambda_{\mathrm{ex}} = 310$ nm, $\lambda_{\mathrm{em}} = 330$–$550$ nm for DUT-5:$\mathrm{Eu^{3+}}$ and nDUT-5:$\mathrm{Eu^{3+}}$ and $\lambda_{\mathrm{ex}} = 360$ nm, $\lambda_{\mathrm{em}} = 370$–$700$ nm for MOF-253, nMOF-253, MOF-253:$\mathrm{Tb^{3+}}$ and nMOF-253:$\mathrm{Tb^{3+}}$.

Lifetime determinations were carried out by recording the overall luminescence decay times (τ) using a Jobin Yvon Fluorolog 3 with the Data Station (ver. 2.7.4) software for data acquisition and the Decay Analysis Software (ver. 6.8.16) for raw data fitting, respectively, from HORIBA. For this purpose, the instrument was upgraded with a TCSPC (time-correlated single-photon counting) and UV Xenon FX-1102 flashlamp from Excelitas Technologies. However, a pulsed Delta Diode™ 278 nm (HORIBA) was necessary for linker emission decay determination. Moreover, for this method, the sample was filled into a cylindrical synthetic-quartz glass cuvette (proQuarz) and placed in the focus of the beam. Subsequently after recording the overall emission decay, the lifetime has been calculated by exponentially fitting the data with $I(t) = A + B_1 \cdot \mathrm{e}^{-(t-t_0/\tau_1)} + B_2 \cdot \mathrm{e}^{-(t-t_0/\tau_2)}$, where $I(t)$ is the emission intensity depending on time, A is the baseline factor, B is the pre-exponential factor, t_0 is the time offset, t is the time and τ is the lifetime.

Phosphorescence spectra were recorded using a pulsed UV Xenon FX-1102 flashlamp from Excelitas Technologies, each 41 ms a flash. Specimens were cooled down and measured at 77 K inside a specialized Dewar filled with liquid nitrogen. Parameters such as recording delay time, sample window time or counts per flash varied and are given next to the recorded spectra. Subsequently, triplet state determination carried out by using the software OriginPro 2023 (ver. 10.0.0.154) from OriginLab. The intersection of two linear fits marks the triplet state energy.

Organic elemental analysis (OEA). The determinations (wt%) of carbon, hydrogen, and nitrogen were performed with a FlashEA 1112 Series from Thermo Fisher Scientific. The amount of sample was weighed using a UMX-2 scale from METTLER TOLEDO, poured into a tin crucible and burned.

Differential thermoanalysis/thermogravimetry – mass spectrometry (DTA/TG-MS). Thermal properties were simultaneously determined regarding differential thermal analysis and thermogravimetry using a STA 409 PC coupled to a QMS 403 Aëolos Quadro mass spectrometer from NETZSCH. The sample (20–25 mg) was filled into a corundum crucible and heated up to 1000 °C with a heating rate of 5 °C min^{-1}. Argon (20 mL min^{-1}) was used as a protective gas and synthetic air (30 mL min^{-1}) as working gas. MS signals were recorded *via* the quasi-multiple ion detection method (QMID).

Conflicts of interest

There are no conflicts to declare.

Acknowledgements

This work is generously funded by the Deutsche Forschungsgemeinschaft (DFG) within the project MU-1562/13-1 within the priority program SPP-1928 “COORNETs”.

References

1 L. Mu, B. Liu, H. Liu, Y. Yang, C. Sun and G. Chen, *J. Mater. Chem.*, 2012, **22**, 12246.

2 D. Alezi, Y. Belmabkhout, M. Suyetin, P. M. Bhatt, L. J. Weseliński, V. Solovyeva, K. Adil, I. Spanopoulos, P. N. Trikalitis, A. H. Emwas and M. Eddaoudi, *J. Am. Chem. Soc.*, 2015, **137**, 13308–13318.

3 S. Denning, A. A. Majid, J. M. Lucero, J. M. Crawford, M. A. Carreon and C. A. Koh, *ACS Appl. Mater. Interfaces*, 2020, **12**, 53510–53518.

4 Z. He, Y. Dai, X. Li, D. Guo, Y. Liu, X. Huang, J. Jiang, S. Wang, G. Zhu, F. Zhang, L. Lin, J.-J. Zhu, G. Yu and X. Chen, *Small*, 2019, **15**, 1804131.

5 A. Wagner, Q. Liu, O. L. Rose, A. Eden, A. Vijay, Y. Rojanasakul and C. Z. Dinu, *Int. J. Nanomed.*, 2019, **14**, 7583–7591.

6 S. A. Ahmed, M. Nur Hasan, D. Bagchi, H. M. Altass, M. Morad, I. I. Althagafi, A. M. Hameed, A. Sayqal, A. E. R. S. Khder, B. H. Asghar, H. A. Katouah and S. K. Pal, *R. Soc. Open Sci.*, 2020, **7**, 200959.

7 R. Van Zeeland, X. Li, W. Huang and L. M. Stanley, *RSC Adv.*, 2016, **6**, 56330–56334.

8 A. Herbst, A. Khutia and C. Janiak, *Inorg. Chem.*, 2014, **53**, 7319–7333.

9 S. Aguado, J. Canivet and D. Farrusseng, *J. Mater. Chem.*, 2011, **21**, 7582.

10 A. D. Pournara, A. Margariti, G. D. Tarlas, A. Kourtelaris, V. Petkov, C. Kokkinos, A. Economou, G. S. Papaefstathiou and M. J. Manos, *J. Mater. Chem. A*, 2019, **7**, 15432–15443.

11 M. Wickenheisser, T. Paul and C. Janiak, *Microporous Mesoporous Mater.*, 2016, **220**, 258–269.

12 Z. Chen, P. Li, X. Zhang, P. Li, M. C. Wasson, T. Islamoglu, J. F. Stoddart and O. K. Farha, *J. Am. Chem. Soc.*, 2019, **141**, 2900–2905.

13 K. Müller-Buschbaum, F. Beuerle and C. Feldmann, *Microporous Mesoporous Mater.*, 2015, **216**, 171–199.

14 V. Chernikova, O. Yassine, O. Shekhah, M. Eddaoudi and K. N. Salama, *J. Mater. Chem. A*, 2018, **6**, 5550–5554.

15 L. J. Small, S. E. Henkelis, D. X. Rademacher, M. E. Schindelholz, J. L. Krumhansl, D. J. Vogel and T. M. Nenoff, *Adv. Funct. Mater.*, 2020, **30**, 2006598.

16 H. Yang, B. Liu, J. Bright, S. Kasani, J. Yang, X. Zhang and N. Wu, *ACS Appl. Energy Mater.*, 2020, **3**, 4007–4013.

17 S.-S. Liu, Z. Han, J.-S. Yang, S.-Z. Huang, X.-Y. Dong and S.-Q. Zang, *Inorg. Chem.*, 2020, **59**, 396–402.

18 Z. Wei, R. Maile, L. M. Riegger, M. Rohnke, K. Müller-Buschbaum and J. Janek, *Batteries Supercaps*, 2022, **5**(12), e202200318.

19 R. Freund, O. Zaremba, G. Arnauts, R. Ameloot, G. Skorupskii, M. Dincă, A. Bavykina, J. Gascon, A. Ejsmont, J. Goscianska, M. Kalmutzki, U. Lächelt, E. Ploetz, C. S. Diercks and S. Wuttke, *Angew. Chem., Int. Ed.*, 2021, **60**, 23975–24001.

20 L. V. Meyer, F. Schönfeld, A. Zurawski, M. Mai, C. Feldmann and K. Müller-Buschbaum, *Dalton Trans.*, 2015, **44**, 4070–4079.

21 K. Xu, F. Wang, S. Huang, Z. Yu, J. Zhang, J. Yu, H. Gao, Y. Fu, X. Li and Y. Zhao, *RSC Adv.*, 2016, **6**, 91741–91747.

22 K. Mandel, T. Granath, T. Wehner, M. Rey, W. Stracke, N. Vogel, G. Sextl and K. Müller-Buschbaum, *ACS Nano*, 2017, **11**, 779–787.

23 W. T. Carnall, in *Non-metallic Compounds – I*, 1979, vol. 3, pp. 171–208.

24 R. E. Whan and G. A. Crosby, *J. Mol. Spectrosc.*, 1962, **8**, 315–327.

25 S. I. Weissman, *J. Chem. Phys.*, 1942, **10**, 214–217.

26 F. Luo and S. R. Batten, *Dalton Trans.*, 2010, **39**, 4485.

27 T. N. Nguyen, S. V. Eliseeva, A. Gładysiak, S. Petoud and K. C. Stylianou, *J. Mater. Chem. A*, 2020, **8**, 10188–10192.

28 K. A. White, D. A. Chengelis, K. A. Gogick, J. Stehman, N. L. Rosi and S. Petoud, *J. Am. Chem. Soc.*, 2009, **131**, 18069–18071.

29 M. Naito, T. Yokoyama, K. Hosokawa and K. Nogi, in *Nanoparticle Technology Handbook*, Elsevier Science, 2018, pp. 3–44.

30 F. Martinez-Julian, A. Guerrero, M. Haro, J. Bisquert, D. Bresser, E. Paillard, S. Passerini and G. Garcia-Belmonte, *J. Phys. Chem. C*, 2014, **118**, 6069–6076.

31 S. S. El-Deen, A. M. Hashem, A. E. Abdel Ghany, S. Indris, H. Ehrenberg, A. Mauger and C. M. Julien, *Ionics*, 2018, **24**, 2925–2934.

32 D.-H. Ha, M. A. Islam and R. D. Robinson, *Nano Lett.*, 2012, **12**, 5122–5130.

33 Y. L. F. Musico, C. M. Santos, M. L. P. Dalida and D. F. Rodrigues, *ACS Sustain. Chem. Eng.*, 2014, **2**, 1559–1565.

34 W. Wanas, S. A. Abd El-Kaream, S. Ebrahim, M. Soliman and M. Karim, *Sci. Rep.*, 2023, **13**, 27.

35 G. Prencipe, S. M. Tabakman, K. Welsher, Z. Liu, A. P. Goodwin, L. Zhang, J. Henry and H. Dai, *J. Am. Chem. Soc.*, 2009, **131**, 4783–4787.

36 S. L. Pal, U. Jana, P. K. Manna, G. P. Mohanta and R. Manavalan, *J. Appl. Pharm. Sci.*, 2011, **1**, 228–234.

37 M. Naito, T. Yokoyama, K. Hosokawa and K. Nogi, in *Nanoparticle Technology Handbook*, Elsevier Science, 2018, pp. 49–105.

38 J. Andreo, R. Ettlinger, O. Zaremba, Q. Peña, U. Lächelt, R. F. De Luis, R. Freund, S. Canossa, E. Ploetz, W. Zhu, C. S. Diercks, H. Gröger and S. Wuttke, *J. Am. Chem. Soc.*, 2022, **144**, 7531–7550.

39 C. D. Ma, C. Wang, C. Acevedo-Vélez, S. H. Gellman and N. L. Abbott, *Nature*, 2015, **517**, 347–350.

40 X.-G. Wang, Q. Cheng, Y. Yu and X.-Z. Zhang, *Angew. Chem., Int. Ed.*, 2018, **57**, 7836–7840.

41 T. Kundu, S. Mitra, P. Patra, A. Goswami, D. Díaz Díaz and R. Banerjee, *Chem. – Eur. J.*, 2014, **20**, 10514–10518.

42 R. Nagarajan and E. Ruckenstein, *Langmuir*, 1991, **7**, 2934–2969.

43 X. Guo, G. Zhu, F. Sun, Z. Li, X. Zhao, X. Li, H. Wang and S. Qiu, *Inorg. Chem.*, 2006, **45**, 2581–2587.

44 I. Senkovska, F. Hoffmann, M. Fröba, J. Getzschmann, W. Böhlmann and S. Kaskel, *Microporous Mesoporous Mater.*, 2009, **122**, 93–98.

45 E. D. Bloch, D. Britt, C. Lee, C. J. Doonan, F. J. Uribe-Romo, H. Furukawa, J. R. Long and O. M. Yaghi, *J. Am. Chem. Soc.*, 2010, **132**, 14382–14384.

46 M. J. Neufeld, H. Winter, M. R. Landry, A. M. Goforth, S. Khan, G. Pratx and C. Sun, *ACS Appl. Mater. Interfaces*, 2020, **12**, 26943–26954.

47 X. Deng, J. Albero, L. Xu, H. García and Z. Li, *Inorg. Chem.*, 2018, **57**, 8276–8286.

48 S. Chhetri, N. Adak, P. Samanta, N. Murmu and T. Kuila, *J. Compos. Sci.*, 2018, **2**, 37.

49 Y. Yuan, W. Wang, L. Qiu, F. Peng, X. Jiang, A. Xie, Y. Shen, X. Tian and L. Zhang, *Mater. Chem. Phys.*, 2011, **131**, 358–361.
50 C. Wang, J. Kim, J. Tang, M. Kim, H. Lim, V. Malgras, J. You, Q. Xu, J. Li and Y. Yamauchi, *Chem*, 2020, **6**, 19–40.
51 X. Xia, J. Zeng, L. K. Oetjen, Q. Li and Y. Xia, *J. Am. Chem. Soc.*, 2012, **134**, 1793–1801.
52 Z. Haghi and S. M. Masoudpanah, *J. Sol-Gel Sci. Technol.*, 2019, **91**, 335–341.
53 Y. K. Du, P. Yang, Z. G. Mou, N. P. Hua and L. Jiang, *J. Appl. Polym. Sci.*, 2006, **99**, 23–26.
54 P. Horcajada, F. Salles, S. Wuttke, T. Devic, D. Heurtaux, G. Maurin, A. Vimont, M. Daturi, O. David, E. Magnier, N. Stock, Y. Filinchuk, D. Popov, C. Riekel, G. Férey and C. Serre, *J. Am. Chem. Soc.*, 2011, **133**, 17839–17847.
55 J. V Alemán, A. V Chadwick, J. He, M. Hess, K. Horie, R. G. Jones, P. Kratochvíl, I. Meisel, I. Mita, G. Moad, S. Penczek and R. F. T. Stepto, *Pure Appl. Chem.*, 2007, **79**, 1801–1829.
56 K. Binnemans, *Coord. Chem. Rev.*, 2015, **295**, 1–45.
57 P. A. Tanner, *Chem. Soc. Rev.*, 2013, **42**, 5090.
58 D. Y. Medina-Velazquez, U. Caldiño, A. Morales-Ramirez, J. Reyes-Miranda, R. E. Lopez, R. Escudero, R. Ruiz-Guerrero and M. F. Morales Perez, *Opt. Mater.*, 2019, **87**, 3–10.
59 M. Latva, H. Takalo, V.-M. Mukkala, C. Matachescu, J. C. Rodríguez-Ubis and J. Kankare, *J. Lumin.*, 1997, **75**, 149–169.
60 W. T. Carnall, P. R. Fields and K. Rajnak, *J. Chem. Phys.*, 1968, **49**, 4447–4449.
61 W. T. Carnall, P. R. Fields and K. Rajnak, *J. Chem. Phys.*, 1968, **49**, 4450–4455.
62 Y. Lu and B. Yan, *J. Mater. Chem. C*, 2014, **2**, 7411–7416.
63 A. E. Sedykh, M. Becker, M. T. Seuffert, D. Heuler, M. Maxeiner, D. G. Kurth, C. E. Housecroft, E. C. Constable and K. Müller-Buschbaum, *ChemPhotoChem*, 2023, **7**, e202200244.